Measuring Changes in Electrical Impedance During Cell-Mediated Mineralization

Rafael Ramos, MS,[1,2,*] Kairui Zhang, MS,[1,2,*] David Quinn, BS,[1,2] Stephen W. Sawyer, PhD,[1,2]
Shannon Mcloughlin, BS,[1,2] and Pranav Soman, PhD[1,2]

Abstract

Background: The fundamental electrical properties of bone have been attributed to the organic collagen and the inorganic mineral component; however, contributions of individual components within bone tissue toward the measured electrical properties are not known. In our study, we investigated the electrical properties of cell-mediated mineral deposition process and compared our results with cell-free mineralization.

Materials and Methods: Saos-2 cells encapsulated within gelatin methacrylate (GelMA) hydrogels were chemically stimulated in osteogenic medium for a period of 4 weeks. The morphology, composition, and mechanical properties of the mineralized constructs were characterized using bright-field imaging, scanning electron microscopy (SEM) energy-dispersive X-ray spectroscopy, Fourier-transform infrared spectroscopy (FITR), nuclear magnetic resonance spectroscopy (NMR), micro-CT, immunostaining, and mechanical compression tests. In parallel, a custom-made device was used to measure the electrical impedance of mineralized constructs. All results were compared with cell-free GelMA hydrogels mineralized through the simulated body fluid approach.

Results: Results demonstrate a decrease in the electrical impedance of deposited mineral in both cell-mineralized and cell-free mineralized samples.

Conclusions: This study establishes a model system to investigate *in vivo* and *in vitro* mineralization processes.

Keywords: simulated body fluid, mineral deposition, hydrogels, gelatin methacrylate, electrical impedance

Introduction

NATIVE BONE IS A COMPOSITE MATERIAL that consists of highly ordered organic collagen fibrils and inorganic hydroxyapatite (HA) and calcium phosphate mineral.[1] Based on physiological loading, age, and several other parameters, bone is continuously remodeled throughout our lifespan to maintain homeostasis through an intricate process involving bone resorption by osteoclasts and mineral deposition by osteoblasts.[2] The process of mineral deposition by osteoblasts begins with the aggregation of amorphous calcium phosphate within intracellular vesicles, followed by exocytosis of the vesicles into the extracellular space where they begin to deposit crystalline apatite mineral within and along aligned collagen fibrils before crystallizing into HA.[3,4] Understanding the properties of cell-deposited mineral is important as a loss in mineral is often associated with an increased risk of osteoporotic fracture and a reduced rate of bone healing.[5,6] As a result, several research groups have used cell-laden hydrogels as model *in vitro* systems to in-

vestigate the process of mineral deposition.[7–14] In a typical study, osteogenic cells are encapsulated within a hydrogel matrices using cell-friendly crosslinking conditions and chemically induced to facilitate cell-mediated mineral deposition within the hydrogel matrix. For these studies, model cell lines such as human osteogenic sarcoma cells (Saos-2),[9] MC3T3-E1 murine osteoblasts,[15] mesenchymal and adipose stem cells,[16] embryonic stem cells,[17,18] and human-induced pluripotent stem cells[19] have been encapsulated within model natural hydrogels (collagen, fibrin, and alginate), synthetic hydrogels (polyethylene glycol), and semisynthetic hydrogels.[14,20,21] Although studies have investigated the changes in morphology and material composition of mineral deposited by the encapsulated cells, no study has investigated their electrical properties.

Electrical properties have been measured in native bone tissue.[22–26] In fact, clinical therapies based on electric stimulation have shown to enhance bone regeneration.[23,27,28] The origins of electrical properties have been linked to both the organic (type I collagen) and the inorganic (HA) components

---
[1]Department of Biomedical and Chemical Engineering, Syracuse University, Syracuse, New York.
[2]Syracuse Biomaterial Institute, Syracuse, New York.
*Cofirst authors.

of bone tissue, although the exact mechanisms are not known.[26,29–31] In this study, we seek to investigate whether cell-mediated mineralization within a collagen-like hydrogel matrix causes a change in the electrical properties of the hydrogel matrix. To do so, we encapsulated widely used osteoblast-like Saos-2 cells within gelatin methacrylate (GelMA) hydrogels, a denatured form of collagen. Saos-laden GelMA constructs were then chemically stimulated for a period of 28 days, and properties such as mineral morphology, modulus, material composition, and electrical impedance were characterized at different time points. As a cell-free control, GelMA samples mineralized through the simulated body fluid (SBF) method were used. This study provides new data on the changes in the electrical impedance properties during both cell-mediated and cell-free mineralization processes.

Materials and Methods

Design and fabrication of polydimethylsiloxane molds

Mold negatives were designed using Fusion360 CAD software. Acrylonitrile butadiene styrene (ABS) thermoplastic molds with rectangular pit dimensions of 4.9 mm long, 2.9 mm wide, and 0.5 mm high were printed using a Zortrax M200 high-resolution extrusion printer (Fig. 1A). Polydimethylsiloxane (PDMS) (10:1 base:curing agent) was then mixed and cast onto the printed molds and subsequently cured at 60°C for 4 h after degassing under vacuum. Individual rectangular constructs were then cut using a sterile X-acto knife.

GelMA synthesis

Ten grams of type A porcine skin gelatin (Sigma) was dissolved into 100 mL of Dulbecco's phosphate buffered saline (Gibco) at 60°C and stirred until fully dissolved. Eight milliliters of methacrylic anhydride (Sigma) was then slowly added dropwise under continuous stirring conditions. The mixture was then allowed to react for 3 h at 60°C. The mixture was then dialyzed against distilled water using 12–14 kDa dialysis tubing for 1 week at 50°C. The solution was lyophilized for 1 week to generate the GelMA macromer and stored at −80°C until use.

Cell culture and encapsulation within PDMS molds

Human osteosarcoma cells (Saos-2; ATCC) were employed as model osteoblast-like cells for encapsulation experiments. Cells were cultured using Dulbecco's modified Eagle's medium (DMEM) (Life Technologies) with 10% fetal bovine serum (v/v) (Atlanta Biologics), 1% penicillin–streptomycin (Life Technologies), and 1% GlutamMAX (Life Technologies). Cells were routinely passaged as per the manufacturer's protocol with 0.25% trypsin-EDTA (Life Technologies) and stored at 37°C with 5% CO_2. After counting, centrifuged cells were resuspended in DMEM to yield a final concentration of 2.5×10^6 cells/mL. This cell solution was then mixed with sterile-filtered 20% w/v GelMA containing 0.5% Irgacure 2959, resulting in 20 μL aliquots of 10% GelMA containing ∼50,000 cells. The 20 μL aliquots of GelMA-cell prepolymer solution were then carefully pipetted into a sterile PDMS mold. Each sample was then UV cured for 1 min using a handheld Hamamatsu LED Controller (output power 5 mW/cm²; Hamamatsu C11924-511; Hamamatsu Photonics K.K., Japan) (Fig. 1B, C). After curing, samples were removed from the mold and transferred into 24-well plates. Cell-laden GelMA constructs were chemically stimulated using osteogenic medium consisting of DMEM containing 10 nM dexamethasone (DEX, Sigma Aldrich), 100 μM of L-ascorbic acid-2-phosphate (AA2P; Sigma Aldrich), and 5 mM of β-glycerophosphate (βGP; Sigma Aldrich). Chemical stimulation began 24 h after encapsulation and was continued for a period of 28 days. Medium was replaced every 2–3 days.

Compression modulus

The compressive modulus of mineralized cell-laden GelMA constructs was evaluated using a dynamic mechanical analysis machine (Q800; TA Instruments, Inc.) at days 1, 7, 14, 21, and 28. For all constructs, strain percentage was increased from 0 to 40% with a preloaded force of 0.01 N and displacement of 10 μm. The slope of the stress–strain curve from 0 to 10% strain was used to report the compressive modulus as per previous protocols studying GelMA constructs[32] ($n = 3$ for each time point).
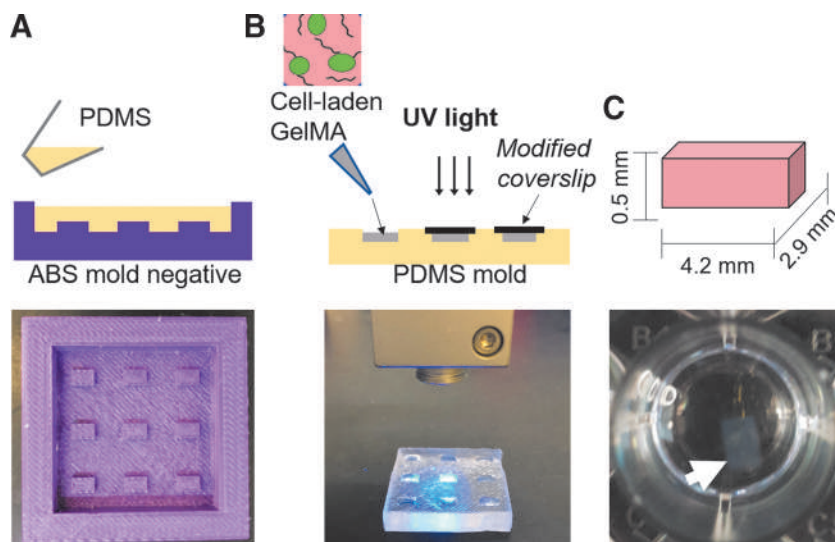
FIG. 1. Process flow used to fabricate mineralized GelMA constructs. **(A)** Schematic of PDMS replica molding process using a 3D printer ABS negative mold (Picture). **(B)** A 10% GelMA with 0.25% Irgacure was casted into PDMS mold and photo-crosslinked using UV light to obtain uniform size GelMA blocks. **(C)** Crosslinked GelMA blocks were incubated in SBF to undergo mineralization. 3D, three-dimensional; ABS, acrylonitrile butadiene styrene; GelMA, gelatin methacrylate; PDMS, polydimethylsiloxane; SBF, simulated body fluid.

Cellular viability and fluorescent staining

Live–dead staining of encapsulated constructs was carried out to observe the viability of encapsulated cells on days 1 and 7. Viability was measured fluorescently with Calcein-AM (live, 1:2000 dilution; Life Technologies) and ethidium homodimer (dead, 1:500 dilution; Life Technologies) and visualized with an inverted fluorescent microscope (Zeiss Axiovert 40 CFL). The live and dead cells were counted using Analyze Particles function in Image J. The live and dead channels were split and converted into 8-bit images. The threshold was set to be 20–255 ($n = 3$ for each time point).

Mineralization using simulated body fluid preparation

The $2\times$ modified simulated body fluid (mSBF) solution was prepared through dissolving 10.8 g NaCl, 1 g NaHCO$_3$, 0.852 g Na$_2$CO$_3$, 0.95 g KCl, 0.46 g K$_2$HPO$_4\cdot$3H$_2$O, 0.622 g MgCl$_2\cdot$6H$_2$O, 0.586 g CaCl$_2$, 0.144 g Na$_2$SO$_4$, 17.892 g HEPES, and 100 mL 0.2 M NaOH into 700 mL distilled water.[33,34] The pH of the solution was buffered to 7.4 using a solution of HEPES dissolved in 0.2 M NaOH. After stirring overnight at 37°C, the solution was diluted to a final volume of 1 L and stored at 4°C for up to 2 months. GelMA blocks cast from a prepolymer solution of similar concentration as the cell-containing variants (10% w/v, 0.25% Irgacure 2959) were then incubated in the mSBF solution at 37°C for up to 14 days. The body fluid was refreshed daily to supply a sufficient number of ions in the solution. The minimal required solution volume was by using the formula provided by Takadama ($V_s = S_a/10$), where V_s was the incubation volume and S_a was the surface area of the sample.

Scanning electron microscopy and elemental characterization

Cell-laden GelMA constructs were evaluated on days 1 and 21 using standard protocol. In brief, constructs were fixed in a 4% formaldehyde solution, followed by serial incubation in ethanol baths of increasing concentration (10%, 30%, 50%, 70%, 90%, and 100% v/v in MilliPore water) for 1 h apiece, before drying under vacuum for 24 h. Constructs were mounted on aluminum stubs using double-sided carbon tape, and sputter coated with Au/Pt (Edwards S150A, 45 mA; 60 s). Samples were then analyzed using an EOL JSM-IT100LA scanning electron microscope under high vacuum at both 10 and 15 kV. Energy-dispersive X-ray spectroscopy (EDS) analysis was used to detect calcium and phosphate within the prepared constructs. GelMA constructs after SBF treatment were also evaluated using the process already described.

Fourier-transform infrared spectroscopy and nuclear magnetic resonance spectroscopy

Cell-laden constructs on days 1 and 21, along with fully mineralized SBF constructs, were lyophilized and subsequently ground into powder using mortar and pestle. This powder was mixed with KBr (sample: KBr 1:100 w/w) and pressed into pellets. The Fourier-transform infrared spectroscopy (FTIR) spectra were recorded with a Nicolet IR 200 (ThermoFisher) at room temperature from 350 to 4000 cm^{-1} with a resolution of 4 cm^{-1} using 16 scans. For obtaining nuclear magnetic resonance spectroscopy (NMR) data, cell-laden constructs on days 1 and 28 were lyophilized and carefully ground into a fine powder using mortar and pestle to ensure they could be placed in a zirconium rotor. Spectra were recorded using a Bruker 300 DPX instrument with a 7 mm CPMAS probe (spin rate 7000 Hz, CP pulse 5.8 μs, delay 5 s, $n = 1$). Topspin was used to analyze the data. Data were obtained in triplicates for each time point.

Histological analysis

Cell-laden constructs were sectioned for mineral on days 7, 14, 21, and 28. Constructs were first fixed in a 4% formaldehyde solution and subsequently cast and cured in a 10% GelMA solution to obtain 6 mm diameter cylinders that were 1 mm thick. These casts were then soaked in a 30% sucrose solution overnight before freezing in Tissue-tek O.C.T. compound (Electron Microscopy Sciences) within 1 cm^3 molds. Frozen samples were then sectioned into 10 μm slices using a Leica CM3050 cryostat (Leica Biosystems, Germany) at −20°C. For Alizarin Red staining, samples were stained in 40 mM Alizarin Red S pH 4.2 (Sigma Aldrich) for 5 min, dehydrated in 100% ethanol for 20 s, rinsed with xylene, and mounted using Permount (ThermoFisher). Images of the sections were viewed using a Leica EZ4 W microscope with the LAS EZ software. SBF-treated constructs were processed using the process already described.

Micro-CT

A Scanco micro-CT 40 (Scanco Medical AG, Brüttisellen, Switzerland) was used to image and quantify mineral formation in cell-laden and SBF-mineralized constructs. All samples were fixed in a 4% formaldehyde solution and placed in groups of three inside gauze-packed 16 mm diameter micro-CT canisters and kept hydrated with phosphate-buffered saline (PBS) during imaging. The samples were scanned at a 6 μm voxel resolution (55 kV, 145 mA, 200 ms integration time). The scans were digitally contoured using a lower global threshold of 160 mg HA cm^{-3} ($n = 3$ for each time point). Consistency in thresholding between ImageJ and Scanco software was ensured by importing a scan of the Scanco HA quality control phantom into ImageJ and plotting grayscale (ImageJ) values versus HA density. All samples were fixed in formaldehyde (4% for 24 h), washed in PBS, and placed lengthwise in a 16 mm diameter sample holder for micro-CT imaging (micro-CT 40; Scanco Medical AG). Foam spacers were placed between samples, which were kept hydrated with PBS. Samples were imaged at a 16–20 μm isotropic voxel resolution (55 kV, 145 mA, 200 ms integration time).

Impedance measurement

A custom-made impedance testing chip was designed and developed.[35,36] The measurement chip was configured with planar electrodes that are adhered to an FR-4 fiberglass printed circuit board substrate. The chip electrodes were constructed of etched copper 17 μm thick, and subsequently plated with nickel and gold on the surface. The exposed electrodes were connected to wires through copper traces that run underneath electrically insulating film to pads that have wires soldered to them that connect to the data acquisition (DAQ) analog input channel. The analog input channel has a 10 GΩ input impedance with 100 pF capacitance to ground and a sensitivity of 91.6 μV. A 100 kΩ resistor was placed in series with the sensing electrodes and a constant voltage of

1.0 V was applied across the series resistor and the ground electrode of the chip. Alternating current was used in this study to ensure the electrode surface was not damaged. Samples were washed five times in sterile Millipore water before taking measurements ($n = 6$ for each time point). Sample dimensions after casting and crosslinking ensured complete coverage of the parallel electrodes. Inner electrode distance was measured at 2.1 mm, with outer electrode distance measuring at the expected 4.30 mm of the sample.

Inductively coupled plasma mass spectrometry

For SBF-mineralized constructs, inductively coupled plasma mass spectrometry was used to quantify the concentration of calcium and phosphorus across a range of time points. In brief, constructs were taken after 1, 3, 7, 9, and 14 days of incubation and ground into powder using a liquid nitrogen/mortar and pestle technique. A 2% nitric acid solution was used to allow the mineral coat to dissolve into the solution. The ionic components were quantified using a Perkin Elmer 5300DV Inductively Coupled Plasma Optical Emission Spectrometer.

Statistical analysis

Paired t-tests were used to compare values across time points for all experiments.

Results

Generation of cell-mediated mineralized constructs

Figure 1 shows the design and fabrication of GelMA constructs laden with Saos-2 cells (50,000 cells/construct) using replica casting within PDMS molds (Fig. 1C). Constructs were cultured in osteogenic medium for 28 days and mineralization was assessed (Fig. 2A). Bright-field imaging depicts the increase in mineral deposits within the GelMA matrix from days 1 to 28. No mineral was detected on day 1, whereas mineral deposits appear as dark spots on day 14. By

day 21, the mineral deposition spanned the entire thickness of the construct with only the outer regions still showing a Gel-MA matrix with embedded mineral aggregates. By day 28, the mineral deposition covers the entire construct. Despite the size of the construct and small mass of deposited mineral, observable differences in the modulus of the gels were measured (Fig. 1B). On day 1, Saos-laden GelMA samples containing no mineral exhibited a compressive modulus of 9.95 ± 2.36 kPa. As the mineral deposition increased on days 7, 14, 21, and 28, the moduli increased to 10.10 ± 5.67, 12.97 ± 4.77, 19.98 ± 0.72, and 25.09 ± 0.47 kPa, respectively. Paired t-tests results showed a significant increase in compressive modulus over time ($p < 0.01$). The cellular viability was assessed on days 1 and 7 to determine cell death induced by the encapsulation process (Fig. 2C). The results showed 80% viability after 1 day, indicating that the procedural damage was minimal. Also, no significant drop in cell viability was observed after 7 days of culture in osteogenic medium (Fig. 2D), indicating the successful diffusion of nutrients and gases throughout the construct.

Scanning electron microscope morphology and elemental characterization of cell-laden mineralized constructs

Scanning electron microscope (SEM) was used to investigate construct morphology and characterize the composition of accumulated mineral for cell-laden constructs. On day 1, constructs appeared to have a smooth surface at low magnification, with small circular and elliptical bumps spread randomly over the entirety of the observed surfaces (Fig. 3A). Based on EDS analysis, day 1 constructs contained primarily carbon and oxygen (Fig. 3B), which were expected due to the presence of GelMA, as these elements were found over the entire surface. The elemental maps were not able to detect calcium; however, small peaks of phosphorus were detected that could be explained due to the presence of encapsulated Saos-2 cells containing phospholipid bilayers. On day 21, constructs showed
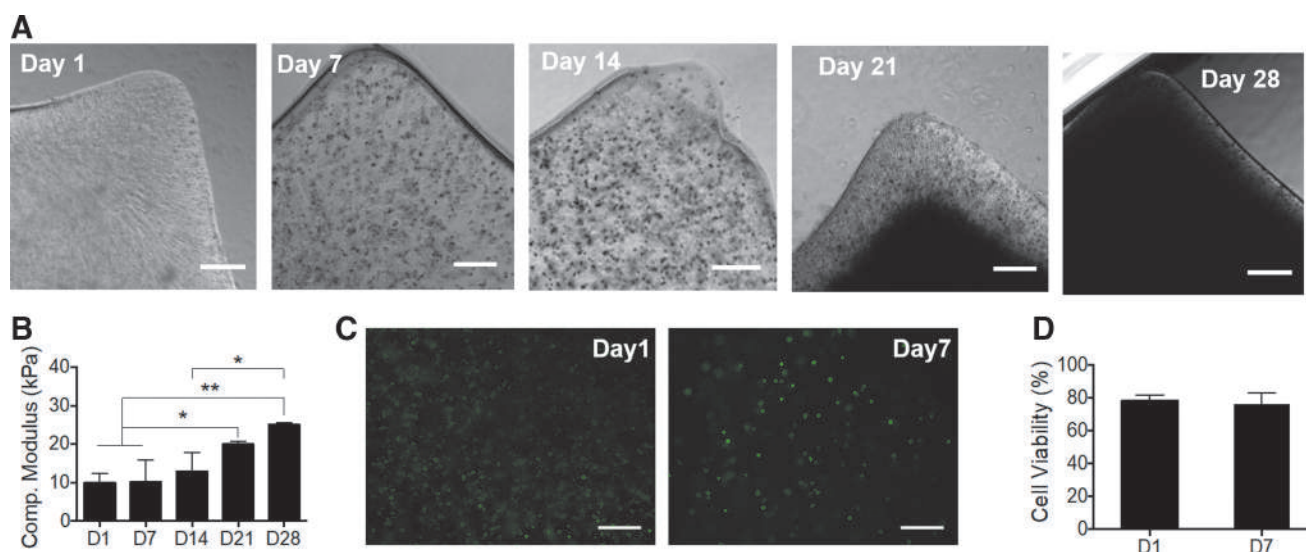
FIG. 2. Characterization of compressive modulus and cell viability test. **(A)** Bright-field images of mineralized cell-laden GelMA on days 1, 14, and 28. Scale bar: 300 μm. **(B)** Compressive modulus of mineralizing samples as a function of total osteogenic stimulation time ($n = 3$, *$p < 0.05$, **$p < 0.01$). **(C)** Representative images of cell viability on days 1 and 7 after encapsulation (scale bar: 300 μm), where no significant decrease in cell viability was detected **(D)** ($n = 3$).
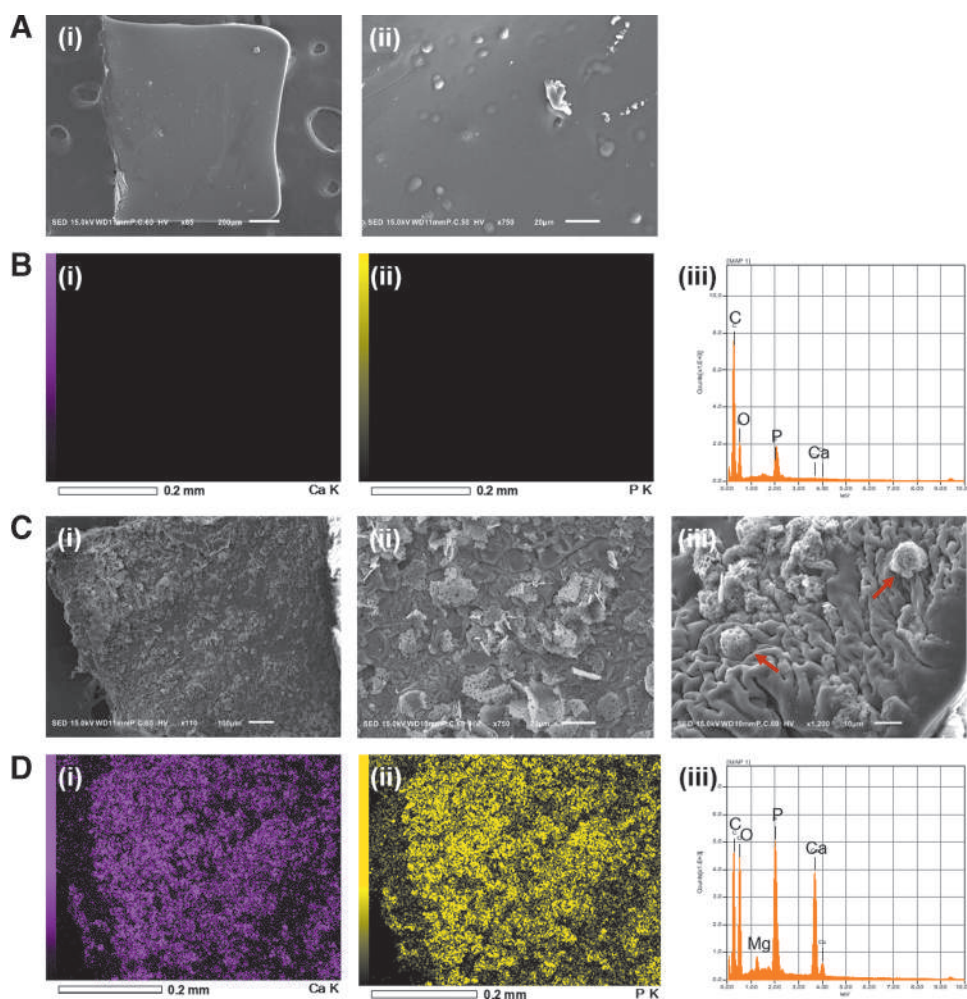
FIG. 3. Surface morphology and elemental characterization of 10% cell-laden GelMA hydrogels. **(A)** Representative images of day 1 constructs. Cell-laden hydrogel surfaces were viewed at **(i)** 65×, **(ii)** 400×. **(B)** EDS analysis of exposed surface of cell-laden hydrogel at 65× magnification. Elemental maps of **(i)** calcium and **(ii)** phosphorus were included to localize elements to their corresponding sites on the recorded image. **(iii)** Corresponding EDS of image highlights the presence of carbon, oxygen, and phosphorus. **(C)** Representative images of day 21 constructs. Overall surface image was taken at **(i)** 110× magnification. **(ii)** Upon closer inspection, these flake irregularities are revealed to be sheets composed of organized white aggregates of apatite mineral. **(iii)** Spherical encapsulated cells were coated in mineral apatite (red arrows). **(D)** EDS analysis of exposed surfaces of mineral-coated cell-laden hydrogel. Elemental maps of **(i)** calcium and **(ii)** phosphorus are included. **(iii)** Corresponding EDS of image highlights the presence of carbon, oxygen, calcium, and phosphorus. EDS, energy-dispersive X-ray spectroscopy.

rough surfaces due to the presence of mineralization (Fig. 3C.i). Higher magnification revealed flake morphology in form of sheets consisting of small spheroids ranging in size from 1 to 5 μm in diameter (Fig. 3C.ii). Meanwhile, images at 1200× magnification showed the colocalization of mineral with other spheroids 10 μm in diameter (Fig. 3C.iii). The calcium phosphate mineralization was mediated by the encapsulated cells and anchored locally to allow for subsequent growth of the mineral crystals. EDS analysis and mapping were able to identify calcium and phosphorus within mineralized constructs (Fig. 3D).

Synthesis and characterization of cell-free mineralized GelMA constructs using SBF method

Replica casting within PDMS master molds was used to fabricate cell-free GelMA 10% (w/v) constructs. Constructs were lyophilized and rehydrated with SBF before being incubated in SBF at 37°C. This allowed the constructs to be hydrated with the ion-saturated solution, ensuring the charged elements were dispersed throughout the gel from the beginning of the soaking step, similar to a previous study. As mineral was deposited within the GelMA constructs, noticeable change in the opaqueness of the constructs is observed, especially after 5 days (Fig. 4A). It was found that mineralization beyond day 14 made the constructs brittle and resulted in their destruction during construct transport or SBF refreshing. Accordingly, day 14 was selected as the end point for this study.

SEM was used to investigate construct morphology and characterize the composition of accumulated mineral for both cell-free constructs. As expected, GelMA constructs not incubated in SBF exhibited a porous structure (Fig. 4B). In contrast, after 14 days of incubation in the SBF, small mineral aggregates covered the entirety of the GelMA surface. The
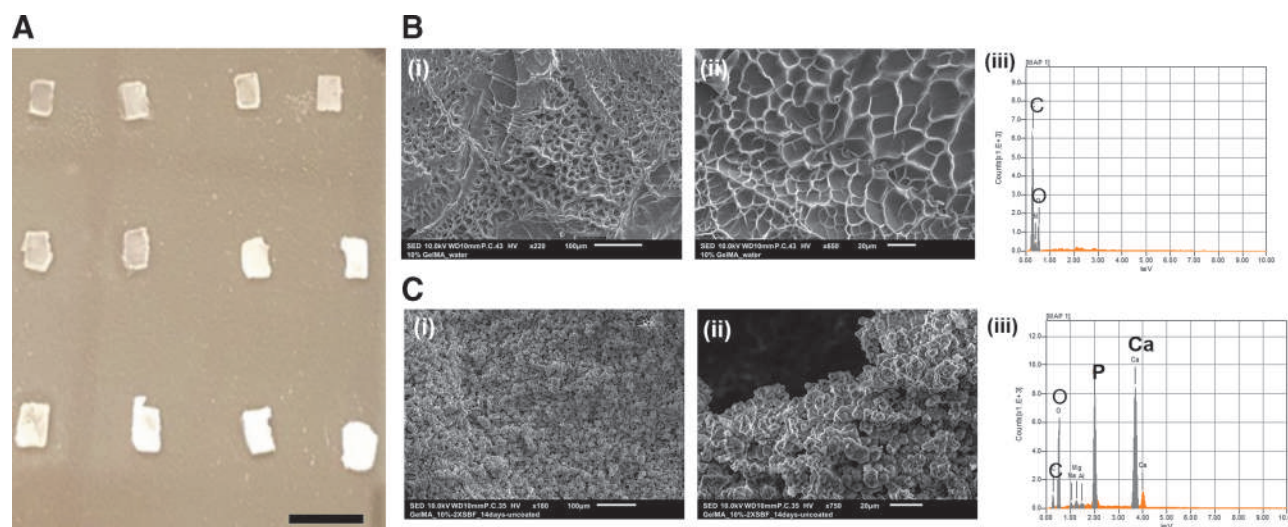
FIG. 4. GelMA apatite mSBF used as mineralized controls. **(A)** Photographic image of gradually mineralized samples from continued incubation in SBF for days 1–4 (row 1), days 5–8 (row 2), and days 9, 10, 12, and 14 (row 3, left to right). By day 7 the GelMA constructs appear to be fully mineralized. Scale bar: 8 mm. **(B) (i, ii)** Representative surface images of unmineralized GelMA constructs at different magnifications, **(iii)** EDS map of unmineralized GelMA surface detects carbon and oxygen. **(C) (i, ii)** Representative images of GelMA constructs after 14 days incubation in SBF at different magnifications. **(iii)** EDS map of mineralized construct surface detects carbon, oxygen, calcium, and phosphorus. mSBF, modified simulated body fluid.

aggregate's shape was irregular but appeared spherical at the smallest units, measuring $\sim 5\,\mu$m in diameter. EDS analysis of unmineralized GelMA constructs detected only carbon and oxygen, whereas constructs incubated in SBF detected calcium and phosphorus and greater levels of carbon (Fig. 4B.iii). These data indicate that SBF precipitated mineral to be a form of apatite. EDS also detected small concentrations of magnesium and sodium, which was expected given their high concentration in SBF. Previous studies with SBF indicated that the morphology of the expected precipitates would be small spheroid units that grew off one another on available hydrogel surfaces.[37,38]

Characterization of mineralized constructs using FTIR

Cell-mediated mineralized constructs. FTIR spectra of nonmineralized and mineralized constructs showed clear differences. Nonmineralized GelMA constructs (10% w/v + 0.25% Ig2959) exhibited the expected amide bands characteristic of gelatin, including N–H stretching at 3425 cm^{-1} for amide A, C–H stretching at 3063 cm^{-1} for amide B, C=O stretching at 1655 cm^{-1} for amide I, N–H deformation at 1543 cm^{-1} for amide II, and N–H deformation at 1278 cm^{-1} for amide III band.[39] After mineralization, new bands associated with HA were observed, particularly the peaks characteristic of PO$_4$ (Fig. 5A). These include bending modes at 603 (v2) and 562 cm^{-1} (v3) and the antisymmetric stretching vibration at 1055 cm^{-1} (v1). These peaks are characteristic of the orthophosphate structure expected of HA.[40,41] NMR of phosphorus (^{31}P CPMAS) was also used to observe the differences between nonmineralized and mineralized constructs (Supplementary Fig. S1). As expected, an unmineralized construct, without any osteogenic induction, did not show any significant traces of phosphorus. The lone peak in the mineralized cell-laden sample exhibited a small shift calculated to
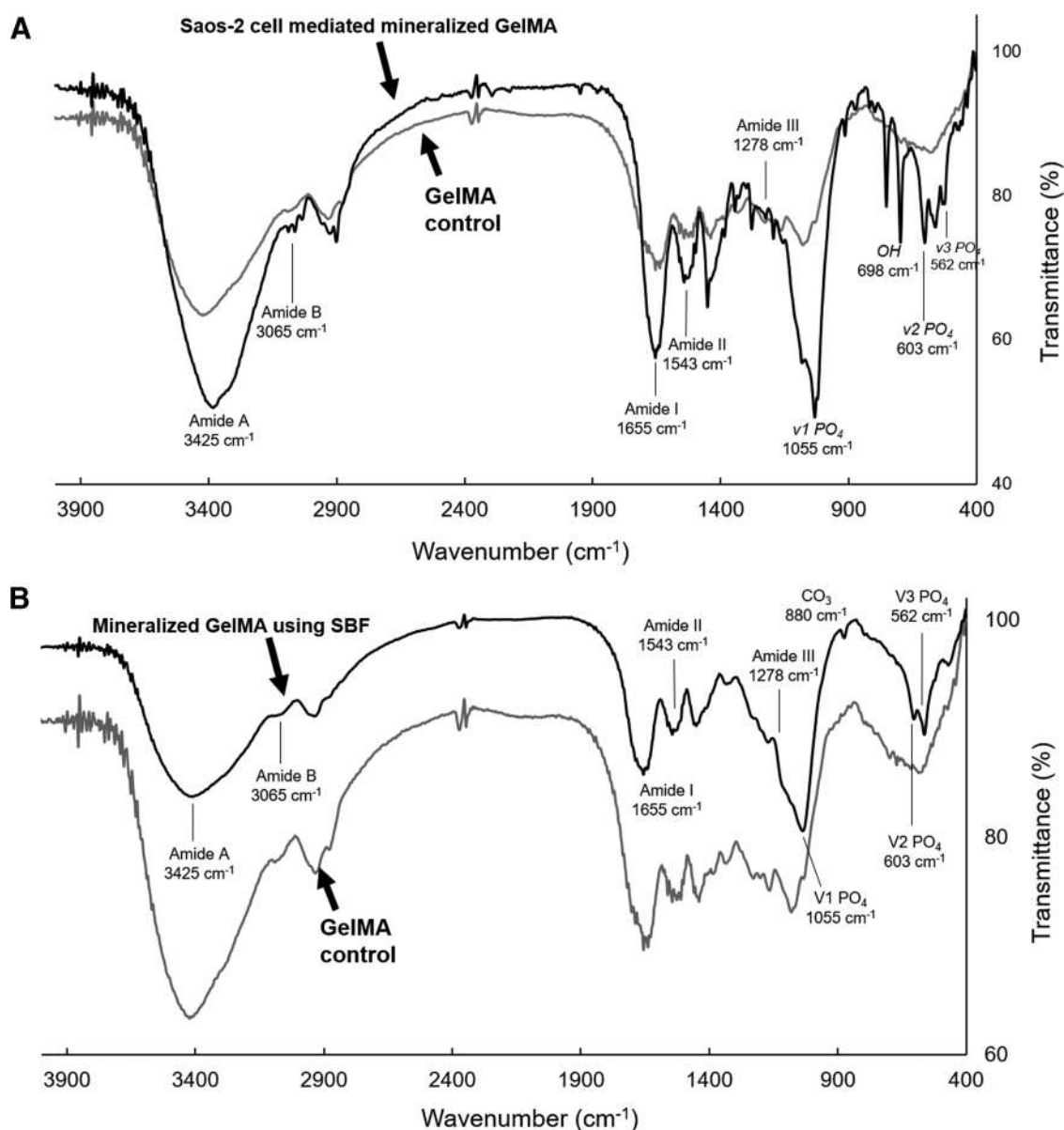
be −5.24 ppm. This small peak range was expected to describe the phosphorus in the PO$_4^{3-}$ ion, the primary anionic building block of HA.[42] This further reinforced the presence of these mineral elements in these stimulated cell-containing constructs.

Cell-free mineralized constructs. When compared with the spectra of GelMA coated in SBF-derived apatite, many of the peaks presented in the same locations, most notably the bending modes at 603 and 562 cm^{-1} and the antisymmetric stretching vibration at 1055 cm^{-1} for PO$_4$ characteristic of the same orthophosphates (Fig. 5B). Despite the relatively weaker signal, a shoulder peak at 880 cm^{-1} also suggested the presence of CO$_3^{2-}$, implying that the minerals generated within constructs were carbonated HA as this would exhibit partial substitution of the phosphate groups with these carbonate groups in the lattice. The absence of hydroxyl peaks was also noted for this SBF apatite.

Characterization of mineralized constructs using Alizarin Red staining

Cell-mediated mineralized constructs. To visualize the presence of calcium produced by encapsulated Saos-2 cells, Alizarin Red staining was used on constructs fixed within a GelMA cast, as described in the Materials and Methods section. On day 28, the constructs stained positively for Alizarin Red stain, confirming that encapsulated cells deposited calcium-based apatite mineral that was homogenously distributed throughout the construct thickness (indicated by dashes; Fig. 6A, B).

Cell-free mineralized constructs. This was contrasted to the calcium deposits produced by sample incubation in 2×mSBF for 7 and 14 days (Fig. 6C, D). At day 7, the outer

A

Saos-2 cell mediated mineralized GelMA

GelMA control

Amide B 3065 cm⁻¹

Amide A 3425 cm⁻¹

Amide III 1278 cm⁻¹

Amide II 1543 cm⁻¹

Amide I 1655 cm⁻¹

OH 698 cm⁻¹

v3 PO₄ 562 cm⁻¹

v2 PO₄ 603 cm⁻¹

v1 PO₄ 1055 cm⁻¹

Transmittance (%)

Wavenumber (cm⁻¹)

B

Mineralized GelMA using SBF

GelMA control

Amide B 3065 cm⁻¹

Amide A 3425 cm⁻¹

Amide II 1543 cm⁻¹

CO₃ 880 cm⁻¹

V3 PO₄ 562 cm⁻¹

Amide III 1278 cm⁻¹

Amide I 1655 cm⁻¹

V2 PO₄ 603 cm⁻¹

V1 PO₄ 1055 cm⁻¹

Transmittance (%)

Wavenumber (cm⁻¹)

FIG. 5. FTIR spectra of hydrogel samples for body fluid and cell-derived mineral apatite samples. **(A)** FTIR spectral overlay of 10% GelMA blocks compared against cell-laden samples osteogenically stimulated for 21 days, **(B)** spectral overlay of 10% GelMA blocks and hydrogels incubated in $2\times$-mSBF after 5 days. The composition of the mineral was not expected to change with increasing mineral masses. FTIR, Fourier-transform infrared spectroscopy.

edges appear red with color decreasing in intensity as the center of the construct. Although minor amounts are present within the bulk, heavier deposition begins occurring after 1 week as the amount of mineral appears to have spread throughout the whole width of the sample by day 14.

Mineral mass quantification and impedance testing

Cell-mediated mineralized constructs. Micro-CT was performed to quantify the mass of mineral deposited by encapsulated cells within the GelMA matrix. On day 7, mineralized mass could not be detected. The three-dimensional (3D) renders visualized the deposited mineral on days 14, 21, and 28 (Fig. 7A). Mineral mass was measured to be 0.173 ± 0.125,

0.492 ± 0.088, and 1.058 ± 0.296 mg for days 14, 21, and 28, respectively (Fig. 7B). Paired t-tests showed the mineral mass significantly increased from days 14 to 28 ($p<0.01$).

A custom-made chip was developed to measure the impedance across the cell-laden hydrogel (Fig. 8A). The system was composed of a DAQ system that measured the voltage drops between the electrodes at given intervals and tracked the changes in the effective impedance of hydrogel constructs over time. Cell-laden GelMA constructs were transferred to the chip for impedance testing at the selected time points (days 1, 7, 14, 21, and 28). Impedance values were found to drop across the testing points, decreasing from 88.26 ± 11.41 kΩ on day 1 to 72.77 ± 23.99 kΩ on day 7, 62.79 ± 17.57 kΩ on day 14, 61.57 ± 13.29 kΩ on day 21, and 37.47 ± 7.44 kΩ on day 28
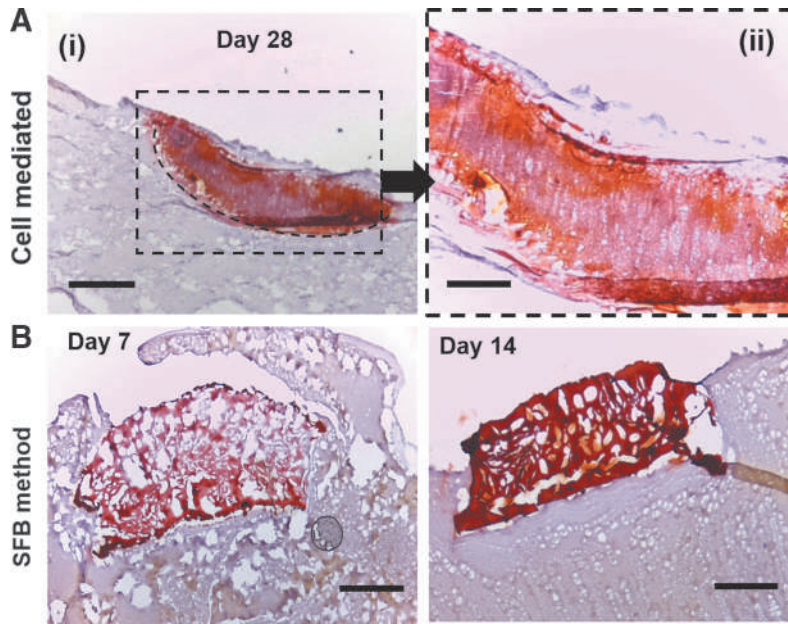
FIG. 6. Alizarin Red staining of mineralized samples. **(A) (i)** Day 28 cell-laden sample encapsulated in 10% GelMA (dash line area). The red stain throughout the sample indicates the presence of calcium-based apatite mineral throughout the whole thickness of the hydrogel. Scale bar: 500 μm. **(ii)** Higher magnification of day 28 sample stained with Alizarin Red. Scale bar: 200 μm. **(B)** Alizarin Red staining of mineralized samples incubated in SBF for 7 and 14 days. Scale bar: 200 μm.

(Fig. 8B). Paired *t*-tests results showed a significant drop in impedance from days 1 to 28 ($p < 0.001$).

Cell-free mineralized constructs. Micro-CT analysis was carried out to quantify the deposition of mineral from precipitated SBF. 3D renders of the scans show that at day 7, the precipitated mineral forms a surface coating on the faces of the gel, while existing primarily as individual aggregates within the bulk of the structure. This mineral scaffold grows into the bulk after an additional 7 days of incubation, with additional deposition occurring along the outer faces of the construct (Fig. 7C). The amount of mineral was only quantified for 7 and 14 days of incubation and was measured at 0.062 ± 0.025 and 0.515 ± 0.034 mg, respectively (Fig. 7D).

Paired *t*-test results showed a significant increase in mineral mass from day 0 to day 14 ($p < 0.001$).

As deposition was expected to occur quickly over time, daily time points were used to track increases in sample conductivity. Control gels hydrated in Millipore water exhibited an impedance of about 570 kΩ, showing that the impedance of GelMA could be modified by the incubation in medium due to the potential deposition of protein and ions. Conductivity increased for the first 4 days of SBF incubation, as impedance values dropped to 331.28 ± 135.22 and 79.25 ± 43.61 kΩ on days 1 and 7, respectively. At the latter point, a plateauing of the average measurements was shown to continue over all subsequent days until day 14 with a value of 47.21 ± 10.05 kΩ (Fig. 8C). This last value was compared with the impedence of fully mineralized cell-laden
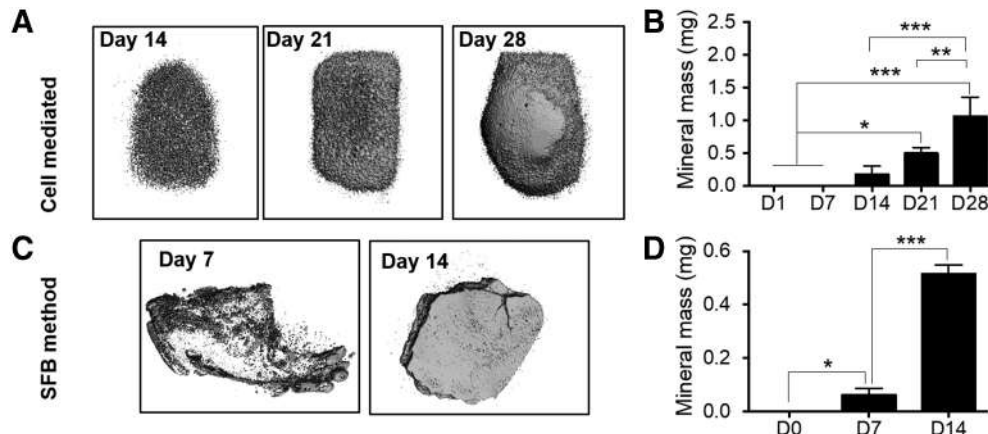

FIG. 7. Comparison of quantified mineral mass and construct impedance as a function of osteogenic induction and incubation times. **(A)** 3D rendered models of micro-CT tomographic scans of mineral-laden constructs at days 14, 21, and 28. Spherical aggregates are widespread throughout the gel at day 14, with fused surfaces becoming apparent by day 21. **(B)** Quantified mineral masses as function of osteogenic incubation time from days 1 to 28 ($n = 3$, *$p < 0.05$, **$p < 0.01$, ***$p < 0.001$). **(C)** 3D rendered models of micro-CT tomographic scans of mineralized samples incubated in SBF at days 7 and 14. **(D)** Quantified mineral mass as a function of SBF incubation time from days 1, 7, and 14 ($n = 3$, *$p < 0.05$, ***$p < 0.001$).
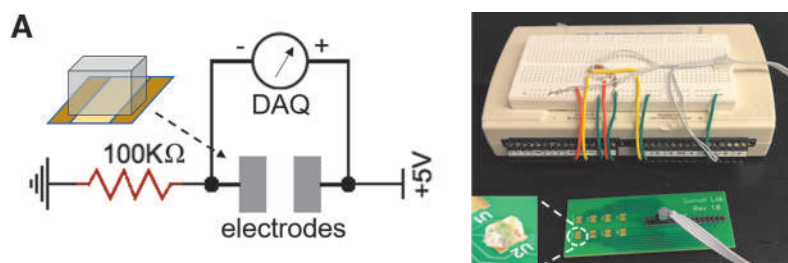
FIG. 8. Electrical impedance measurement of mineralized GelMA constructs. **(A)** Schematic and picture of the impedance testing setup showing the test circuit, custom-made green chip, and LabView DAQ interface. **(B)** Changes in sample impedance as a function of total osteogenic stimulation time ($n=6$, **$p<0.01$, ***$p<0.001$). **(C)** Changes in sample impedance as a function of total SBF incubation time ($n=10$, ***$p<0.001$). **(D)** Tabulated summary of fully mineralized cell-laden and SBF-incubated samples with comparative impedance and mineral mass. DAQ, data acquisition.
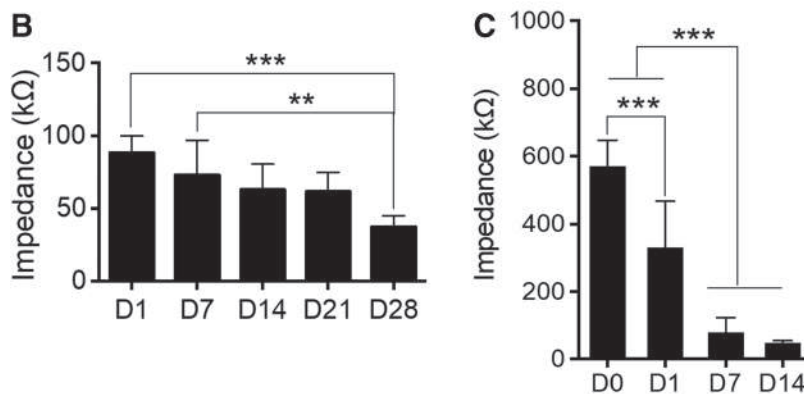
Sample Type	Impedance (kΩ)	Mineral Mass (mg)
Cell-free mineralized GelMA (Day 14)	47.21 ± 10.05	0.515 ± 0.034
Cell-mediated mineralized GelMA (Day 28)	39.02 ± 2.06	1.058 ± 0.296

constructs, even if the mineral density was determined to be different (Fig. 8D).

Discussion

Although electrical stimulation has been used for decades to stimulate bone growth in clinics and for bone tissue engineering applications, the fundamental electrical properties of bone are not completely understood.[22,23,29–31,43–46] Previous studies have suggested that the collagen (organic component) provides localized dipoles, whereas the apatite mineral (inorganic component) provides a path for the conduction of charge throughout the tissue.[37,47,48] A new study has also shown that pure HA exhibited a similar flexoelectricity as bone, suggesting bone mineral largely contributes to the bone electrical property.[44] However, contributions of individual components within bone tissue toward the measured electrical properties are not known. In our study, for the first time, we investigated the electrical properties of cell-mediated mineral deposition process occurring within GelMA hydrogels, and compared our results with cell-free GelMA samples mineralized through the SBF approach. To mimic *in vivo* mineralization of bone tissue that involves the nucleation and growth of calcium phosphate crystals within an organic collagen-based matrix, we choose GelMA and

Saos-2 cells to build a model system. GelMA, a denatured form of collagen, was chosen as model hydrogel due to its widespread use in the field and due to established synthesis, fabrication, and material characterization techniques.[12,35,36] Saos-2, an osteoblast-like cell line, was chosen as it is a widely used cell line that deposits mineral within hydrogel matrix when chemically stimulated, mimicking the process of mineral deposition occurring *in vivo*.[9,12,35]

Bright-field images taken on day 7 showed that the initial deposition of mineral resulted in the formation of isolated aggregates that merged and formed a continuous and partially connected unit with increasing culture durations (days 14, 21, and 28). This provides an explanation of why mineralized constructs on day 7 had compressive moduli closer to the day 1 constructs, as isolated mineral deposits randomly within the GelMA matrix were unable to provide additional resistance against compressive loading. Only after day 14 was a significant increase in modulus observed as the isolated mineral deposits merged to form a continuous structure. By day 28, mineralized constructs exhibited modulus values closer to those found in native osteon matrices (25–40 kPa during compressive loading).[34]

The FTIR results show the existence of PO$_4$ group, which is the unique composition of biological apatite.[45] The peaks at 562/603/1055/3065/3425 cm^{-1} indicate the deposition of

HA crystals after osteogenic induction that are similar to those previously reported in synthetic mineralized GelMA and collagen gels.[34,37,49,50] It should be noted that the SBF-deposited minerals were lacking the hydroxyl group signal seen in the cell-derived apatite. Because this signal would be present if the deposited hydroxyapatite was crystalline in nature, this suggests that the mineral deposited by the SBF is structurally amorphous.

Based on the electrical impedance and mineral mass data, it was found that Saos-laden GelMA constructs became more conductive as mineral mass increased. In addition, the impedance decreases to ~40 kΩ at day 28 that could be attributed to large amounts of mineralization. Our results match with similar studies in the literature. For instance, four-point probes were used to measure the impedance across a range of inner electrode distances, which showed that there exists a linear relationship between inner electrode distance and the obtained impedance across a bone sample, both with and without marrow, with variations existing even between different samples. For inner and outer electrode distances similar to the test chip used in our study (inner: 2.1 mm; outer: 4.3 mm), a corresponding impedance range between 20 and 40 kΩ would be anticipated if measurements from marrowless bone sample were compared with our results. For this consideration, a value of 3.2 mm corresponding to the midpoint distance between the two parallel electrodes would result in an impedance of about 29 kΩ,[51] similar to our results. Other groups have also used custom two-electrode setups to report impedance values of cortical bone measured in the kiloOhm range. Impedance values for trabecular bone were likewise reported in the 10s of kiloOhms range.[52] Despite the similarities in these values, measurement reported in the literature varies depending on bone types used and methodology, with the latter being particularly dependent on the frequency and probe types used.

In our study, the concentrations of AA2P (100 μM), βGP (5 mM), and DEX (10 nM) used in osteogenic medium were adequate for cell-mediated mineral deposition, while causing no precipitation in the absence of cells. Control experiments were performed with Saos-laden GelMA incubated in normal DMEM without osteogenic medium. After 14 days, an impedance of 103.57 ± 6.69 kΩ ($n = 3$) was recorded, suggesting that the observed decrease of impedance in samples incubated in osteogenic medium was due to the mineral deposition by the encapsulated Saos-2 cells.

To check whether the drop in impedance was due to some unique bioelectrical phenomenon occurring during cell-mediated mineralization or was this simply a materials property of the inorganic mineral, cell-free GelMA was mineralized using the SBF method. Previously, protein-based hydrogels were shown to facilitate the deposition of mineral using the SBF method.[53–55] In this method, hydrogel constructs are incubated in a solution containing ionic elements with an equal or similar ion concentration compared with the blood plasma. By controlling the incubation time, hydrogel properties, and solution composition, bone-like apatite mineral is precipitated within the hydrogel matrix. Researchers have used the SBF method with collagen and GelMA hydrogel to create an *in vitro* mineralized control.[19,37,38,56,57] GelMA possesses negatively charged domains that allow for easy precipitation of calcium and other divalent cations onto the surface to initiate the apatite mineral lattice.[33,34,58–63]

Although SBF-mineralized hydrogels have been increasingly used to mimic the inorganic component of bone tissue, little is known about the electrical properties of these mineralized constructs. In this study, SBF-mediated mineralized GelMA constructs served as a cell-free control, and the morphology, modulus, material composition, and electrical impedance properties were compared with constructs mineralized by the Saos-2-mediated deposition processes. Since SBF-mediated mineralized constructs also show a drop in impedance (Supplementary Fig. S2), the electrical property is most likely a purely materials property rather than a bioelectric phenomenon associated with cell-mediated osteogenesis. These results should be carefully interpreted to account for the differences in the chemical composition of the mineral formed by cells against that which is deposited during SBF incubation.

The aim of this study was to establish a model system to investigate whether mineralization results in any changes in the electrical properties of the construct using a cell-mediated (Saos-2 laden GelMA; Supplementary Fig. S3) and cell-free approach (SBF-precipitated GelMA). We acknowledge that the reported results only apply to this specific combination of biomaterial, cell type, and incubation conditions. This model system can be further extended to relevant cell types, such as human mesenchymal stem cells as well as collagen type 1 matrix, to confirm that this reported result of ''mineral deposition decreases electrical impedance'' holds true across cell and matrix types. In addition, this model system can be extended to study whether external electrical stimulation could influence the mineral deposition process in cell-mediated and cell-free SBF-precipitated systems.

Conclusion

The goal of this study was to measure the electrical properties of mineral generated by cell-mediated deposition and cell-free precipitation through the SBF method. Our results show a decrease in the electrical impedance of deposited mineral in both cases, suggesting that cell-mediated processes do not play a role in the measured property, but this electrical property is a fundamental materials property of the inorganic mineral component. Additional experiment with relevant cell types and extracellular matrix should be conducted to confirm this result.

Acknowledgments

Author Disclosure Statement

No competing financial interests exist.

Supplementary Material

Supplementary Figure S1
Supplementary Figure S2
Supplementary Figure S3

References

1. Florencio-Silva R, Sasso GRdS, Sasso-Cerri E, et al. Biology of bone tissue: Structure, function, and factors that influence bone cells. Biomed Res Int 2015;2015:421746.

2. Manolagas SC, Jilka RL. Bone marrow, cytokines, and bone remodeling—Emerging insights into the pathophysiology of osteoporosis. N Engl J Med 1995;332:305–311.

3. Wittkowske C, Reilly GC, Lacroix D, et al. In vitro bone cell models: Impact of fluid shear stress on bone formation. Front Bioeng Biotechnol 2016;4:87.

4. Boonrungsiman S, Gentleman E, Carzaniga R, et al. The role of intracellular calcium phosphate in osteoblast-mediated bone apatite formation. Proc Natl Acad Sci U S A 2012;109:14170–14175.

5. Marshall D, Johnell O, Wedel H. Meta-analysis of how well measures of bone mineral density predict occurrence of osteoporotic fractures. BMJ 1996;312:1254–1259.

6. Hoang-Kim A, Gelsomini L, Luciani D, et al. Fracture healing and drug therapies in osteoporosis. Clin Cases Miner Bone Metab 2009;6:136.

7. Dolatshahi-Pirouz A, Nikkhah M, Gaharwar AK, et al. A combinatorial cell-laden gel microarray for inducing osteogenic differentiation of human mesenchymal stem cells. Sci Rep 2014;4:3896.

8. Man Y, Wang P, Guo Y, et al. Angiogenic and osteogenic potential of platelet-rich plasma and adipose-derived stem cell laden alginate microspheres. Biomaterials 2012;33:8802–8811.

9. Sawyer S, Oest M, Margulies B, et al. Behavior of encapsulated Saos-2 cells within gelatin methacrylate hydrogels. J Tissue Sci Eng 2016;7:2.

10. Burdick JA, Anseth KS. Photoencapsulation of osteoblasts in injectable RGD-modified PEG hydrogels for bone tissue engineering. Biomaterials 2002;23:4315–4323.

11. Chatterjee K, Lin-Gibson S, Wallace WE, et al. The effect of 3D hydrogel scaffold modulus on osteoblast differentiation and mineralization revealed by combinatorial screening. Biomaterials 2010;31:5051–5062.

12. Sawyer SW, Shridhar SV, Zhang K, et al. Perfusion directed 3D mineral formation within cell-laden hydrogels. Biofabrication 2018;10:035013.

13. Fedorovich NE, Alblas J, de Wijn JR, et al. Hydrogels as extracellular matrices for skeletal tissue engineering: State-of-the-art and novel application in organ printing. Tissue Eng 2007;13:1905–1925.

14. Thiele J, Ma Y, Bruekers SMC, et al. 25th anniversary article: Designer hydrogels for cell cultures: A materials selection guide. Adv Mater 2014;26:125–148.

15. Quarles LD, Yohay DA, Lever LW, et al. Distinct proliferative and differentiated stages of murine MC3T3-E1 cells in culture: An in vitro model of osteoblast development. J Bone Miner Res 1992;7:683–692.

16. Benoit DSW, Schwartz MP, Durney AR, et al. Small functional groups for controlled differentiation of hydrogel-encapsulated human mesenchymal stem cells. Nat Mater 2008;7:816.

17. Buttery LDK, Bourne S, Xynos JD, et al. Differentiation of osteoblasts and in vitro bone formation from murine embryonic stem cells. Tissue Eng 2001;7:89–99.

18. Bielby RC, Boccaccini AR, Polak JM, et al. In vitro differentiation and in vivo mineralization of osteogenic cells derived from human embryonic stem cells. Tissue Eng 2004;10:1518–1525.

19. Kang H, Shih Y-RV, Hwang Y, et al. Mineralized gelatin methacrylate-based matrices induce osteogenic differentiation of human induced pluripotent stem cells. Acta Biomater 2014;10:4961–4970.

20. Xavier JR, Thakur T, Desai P, et al. Bioactive nanoengineered hydrogels for bone tissue engineering: A growth-factor-free approach. ACS Nano 2015;9:3109–3118.

21. Carles-Carner M, Saleh LS, Bryant SJ. The effects of hydroxyapatite nanoparticles embedded in a MMP-sensitive photoclickable PEG hydrogel on encapsulated MC3T3-E1 pre-osteoblasts. Biomed Mater 2018;13:045009.

22. Kohata K, Itoh S, Horiuchi N, et al. The role of the collaborative functions of the composite structure of organic and inorganic constituents and their influence on the electrical properties of human bone. Biomed Mater Eng 2016;27:305–314.

23. Hronik-Tupaj M, Kaplan DL. A review of the responses of two-and three-dimensional engineered tissues to electric fields. Tissue Eng Part B Rev 2012;18:167–180.

24. Fukada E, Yasuda I. On the piezoelectric effect of bone. J Phys Soc J 1957;12:1158–1162.

25. Shu Y, Baumann MJ, Case ED, et al. Surface microcracks signal osteoblasts to regulate alignment and bone formation. Mater Sci Eng C 2014;44:191–200.

26. Clarke B. Normal bone anatomy and physiology. Clin J Am Soc Nephrol 2008;3:S131–S139.

27. Bassett CAL, Pawluk RJ, Pilla AA. Acceleration of fracture repair by electromagnetic fields. A surgically noninvasive method. Ann N Y Acad Sci 1974;238:242–262.

28. Ito H, Shirai Y. The efficacy of ununited tibial fracture treatment using pulsing electromagnetic fields. J Nippon Med Sch 2001;68:149–153.

29. Pickering S, Scammell B. Electromagnetic fields for bone healing. Int J Low Extrem Wounds 2002;1:152–160.

30. Sierpowska J, Lammi M, Hakulinen M, et al. Effect of human trabecular bone composition on its electrical properties. Med Eng Phys 2007;29:845–852.

31. McKibbin B. The biology of fracture healing in long bones. J Bone Joint Surg Br 1978;60:150–162.

32. Chen YX, Yang S, Yan J, et al. A novel suspended hydrogel membrane platform for cell culture. J Nanotechnol Eng Med 2015;6:021002.

33. Oyane A, Kim HM, Furuya T, et al. Preparation and assessment of revised simulated body fluids. J Biomed Mater Res A 2003;65:188–195.

34. Kikuchi M, Ikoma T, Itoh S, et al. Biomimetic synthesis of bone-like nanocomposites using the self-organization mechanism of hydroxyapatite and collagen. Compos Sci Technol 2004;64:819–825.

35. Sawyer SW, Dong P, Venn S, et al. Conductive gelatin methacrylate-poly (aniline) hydrogel for cell encapsulation. Biomed Phys Eng Express 2017;4:015005.

36. Wu Y, Chen YX, Yan J, et al. Fabrication of conductive gelatin methacrylate–polyaniline hydrogels. Acta Biomater 2016;33:122–130.

37. Zhou L, Tan G, Tan Y, et al. Biomimetic mineralization of anionic gelatin hydrogels: Effect of degree of methacrylation. RSC Adv 2014;4:21997–22008.

38. Tan G, Zhou L, Ning C, et al. Biomimetically-mineralized composite coatings on titanium functionalized with gelatin methacrylate hydrogels. Appl Surf Sci 2013;279:293–299.

39. Chang MC, Tanaka J. FT-IR study for hydroxyapatite/collagen nanocomposite cross-linked by glutaraldehyde. Biomaterials 2002;23:4811–4818.

40. Tas AC. Calcium metal to synthesize amorphous or cryptocrystalline calcium phosphates. Mater Sci Eng C 2012; 32:1097–1106.

41. Cai MM, Smith ER, Holt SG. The role of fetuin-A in mineral trafficking and deposition. Bonekey Rep 2015;4:672.

42. Sannigrahi P, Ingall E. Polyphosphates as a source of enhanced P fluxes in marine sediments overlain by anoxic waters: Evidence from 31 P NMR. Geochem Trans 2005; 6:52.

43. Liu Y, Wu G, de Groot K. Biomimetic coatings for bone tissue engineering of critical-sized defects. J R Soc Interface 2010;7:S631.

44. Vasquez-Sancho F, Abdollahi A, Damjanovic D, et al. Flexoelectricity in bones. Adv Mater 2018;30:1705316.

45. Hu W-W, Hsu Y-T, Cheng Y-C, et al. Electrical stimulation to promote osteogenesis using conductive polypyrrole films. Mater Sci Eng C 2014;37:28–36.

46. Thrivikraman G, Lee PS, Hess R, et al. Interplay of substrate conductivity, cellular microenvironment, and pulsatile electrical stimulation toward osteogenesis of human mesenchymal stem cells in vitro. ACS Appl Mater Interfaces 2015;7:23015–23028.

47. Habraken WJEM, Tao J, Brylka LJ, et al. Ion-association complexes unite classical and non-classical theories for the biomimetic nucleation of calcium phosphate. Nat Commun 2013;4:1507.

48. Veis A, Dorvee JR. Biomineralization mechanisms: A new paradigm for crystal nucleation in organic matrices. Calcif Tissue Int 2013;93:307–315.

49. Liu Q, Huang S, Matinlinna JP, et al. Insight into biological apatite: Physiochemical properties and preparation approaches. Biomed Res Int 2013;2013.

50. Marelli B, Ghezzi CE, Barralet JE, et al. Collagen gel fibrillar density dictates the extent of mineralization in vitro. Soft Matter 2011;7:9898–9907.

51. Herbst E. Electric stimulation of bone growth and repair: A review of different stimulation methods. Burny F, Herbst E, Hinsenkamp M In: Electric Stimulation of Bone Growth and Repair. Berlin, Germany: Springer, 1978; 1–13.

52. Balmer TW, Vesztergom S, Broekmann P, et al. Characterization of the electrical conductivity of bone and its correlation to osseous structure. Sci Rep 2018;8:8601.

53. Wang Y, Azaïs T, Robin M, et al. The predominant role of collagen in the nucleation, growth, structure and orientation of bone apatite. Nat Mater 2012;11:724.

54. Bigi A, Boanini E, Panzavolta S, et al. Bonelike apatite growth on hydroxyapatite–gelatin sponges from simulated body fluid. J Biomed Mater Res 2002;59:709–715.

55. Zhang L-J, Feng X-S, Liu H-G, et al. Hydroxyapatite/collagen composite materials formation in simulated body fluid environment. Mater Lett 2004;58:719–722.

56. Robin M, Almeida C, Azaïs T, et al. Involvement of 3D osteoblast migration and bone apatite during in vitro early osteocytogenesis. Bone 2016;88:146–156.

57. Uchihashi K, Aoki S, Matsunobu A, et al. Osteoblast migration into type I collagen gel and differentiation to osteocyte-like cells within a self-produced mineralized matrix: A novel system for analyzing differentiation from osteoblast to osteocyte. Bone 2013;52:102–110.

58. Kim S-S, Park MS, Gwak S-J, et al. Accelerated bonelike apatite growth on porous polymer/ceramic composite scaffolds in vitro. Tissue Eng 2006;12:2997–3006.

59. Li J, Liao H, Sjöström M. Characterization of calcium phosphates precipitated from simulated body fluid of different buffering capacities. Biomaterials 1997;18:743–747.

60. Habibovic P, Barrere F, Van Blitterswijk CA, et al. Biomimetic hydroxyapatite coating on metal implants. J Am Ceram Soc 2002;85:517–522.

61. Sa Y, Yang F, de Wijn JR, et al. Physicochemical properties and mineralization assessment of porous polymethylmethacrylate cement loaded with hydroxyapatite in simulated body fluid. Mater Sci Eng C 2016;61:190–198.

62. Mi H-Y, Jing X, Salick MR, et al. Morphology, mechanical properties, and mineralization of rigid thermoplastic polyurethane/hydroxyapatite scaffolds for bone tissue applications: Effects of fabrication approaches and hydroxyapatite size. J Mater Sci 2014;49:2324–2337.

63. Zadpoor AA. Relationship between in vitro apatite-forming ability measured using simulated body fluid and in vivo bioactivity of biomaterials. Mater Sci Eng C 2014;35:134–143.

Address correspondence to:
Pranav Soman, PhD
Department of Biomedical and Chemical Engineering
Syracuse University
318 Bowne Hall
Syracuse, NY 13244-1200

E-mail: psoman@syr.edu